Toward understanding of ion dynamics in highly conductive lithium ion conductors: Some perspectives by solid state NMR techniques

Yu-Xuan Xiang[a], Guorui Zheng[a], Guiming Zhong[a,b], Dawei Wang[a,c], Riqiang Fu[d], Yong Yang[a,*]

[a] State Key Laboratory for Physical Chemistry of Solid Surfaces, Collaborative Innovation Center of Chemistry for Energy Materials and Department of Chemistry, College of Chemistry and Chemical Engineering, Xiamen University, Xiamen 361005, China.
[b] Xiamen Institute of Rare Earth Materials, Chinese Academy of Sciences, Xiamen 361021, China
[c] Department of Mechanical and Materials Engineering, University of Western Ontario, London, Ontario, Canada, N6A 5B8
[d] National High Magnetic Field Laboratory, 1800 E. Paul Dirac Drive, Tallahassee, FL 32310, USA

ARTICLE INFO

ABSTRACT

Solid state lithium ion conductors are promising to replace the organic liquid electrolytes for a safer and long cycle-life lithium battery. However, solid electrolytes are still not fully explored and need extensive basic studies to understand their intrinsic conducting mechanism and interfacial properties between electrodes and electrolytes. In this review, we highlight the latest progresses in the research of lithium ion conductors by using advanced solid state nuclear magnetic resonance(SS NMR) spectroscopy, i.e. Magic angle spinning (MAS) NMR, pulsed-field gradient (PFG) NMR, spin-lattice(SLR) as well as spin-spin relaxation NMR, spin alignment echo (SAE) NMR and two-dimensional exchange (2D EXSY) NMR, and briefly review the application of these solid NMR techniques in LISICON-, NASICON- and Garnet-type lithium ion conductors in the different time/length scales, as well as the measurement in the determination of ion occupancy, ion diffusion pathways, and diffusion coefficients.

1. Introduction

Lithium ion batteries (LIBs) are promising candidates for sustainable energy to replace conventional fossil energy, which caused severe environmental pollutions and carbon dioxide emissions. The demand for sustainable energy is increasing. Improving the energy density of the energy devices is critical, but it cannot be overlooked that the safety of the portable energy storage devices. Nowadays, the commercial lithium-ion batteries using flammable and explosive organic electrolyte, has caused some risky in the large-scale operations of the batteries [1]. As an alternative to commercially dominant liquid organic electrolytes, solid electrolytes have attracted a great deal of attention on both academia and industry due to their good mechanical properties, wide electrochemical windows and good chemical stability, and can greatly improve the safety of lithium-ion batteries. However, the applications of solid-state batteries are mainly limited by its large internal resistance. Therefore, in order to play the advantages of all-solid-state batteries, improving the ionic conductivity of solid electrolyte and reducing the solid interface impedance are the key issues. The prerequisite of solving the above problems is to understand the movement patterns of lithium ions in solids. At present, various complementary techniques have been used to characterize the structure and lithium dynamics of solid electrolytes, such as XRD [2], NPD [3], AC impedance [4–8], and SS-NMR[9–13]etc. Among them, SS-NMR, with the demonstrated ability to detect local structure and ion dynamics of specific nucleuses in the solid electrolytes, is an indispensable characterization method of analyzing ion motions at the atomic level. In this short article, we first briefly introduce a variety of NMR techniques for solid electrolytes, including NMR techniques at different time scales. Then some newest progress in the detection of the ion occupancy at different Li sites and Li^+ migration path, dynamic parameters such as diffusion coefficients by using different SS NMR techniques are also summarized and reviewed.

2. Short introduction to NMR techniques

Local species with different chemical environments such as defects, atomic disorders, and dynamical processes, derive different NMR signals. In return, NMR spectra are sensitive to the local structure of species [14]. As a powerful nondestructive and noncontact technique, NMR is capable of investigating various materials, either crystalline, amorphous or nano-structured materials [9–13].

	Macroscopy	Microscopy
NMR techniques	PFG NMR	NMR relaxation
		SAE NMR
		2D EXSY NMR
		Line widths

2.1. Structural analysis

In solid ionic conductors, ^{6}Li, ^{7}Li, ^{31}P, ^{27}Al. etc. are frequently-used nuclei. As the conductive cations in highly conductive electrolytes, lithium ions are involved in the diffusion pathway directly. Therefore, ^{6}Li/^{7}Li MAS NMR spectra can provide the detailed information about cations distribution with high resolution and sensitivity respectively. Apparently, ^{31}P [8] and ^{27}Al et al. could be employed to investigate the framework and the effects of doping elements on structural changes of the different solid electrolytes.

2.2. Dynamics characterization

On the other side, NMR techniques can be used to probe the Li-ion dynamics directly from macroscopy to microscopy in different length/ time scale (see Table 1) [15–18].

2.2.1. Pulsed-field gradient (PFG) NMR

In terms of macro-dynamics, pulsed-field gradient (PFG) NMR technique has the direct approach to collect self-diffusion coefficients in the range of $10^{-14}\,m^2\,s^{-1}$ to $10^{-11}\,m^2\,s^{-1}$, by fitting the Stejskal-Tanner equation [19,20].

$$M_G(2\tau) = M_0(2\tau)\,exp[-\gamma^2 g^2 \delta^2 D\,(\Delta - \delta/3)] = M_0(2\tau)\,exp(-bD)$$

$$b = -\gamma^2 g^2 \delta^2 (\Delta - \delta/3)$$

where g, δ, and Δ denote the pulse strength, duration time and interval time. Varying g, δ, and Δ, the self-diffusion coefficients can be accessible.

2.2.2. Line width analysis

While microscopic NMR techniques, such as NMR line widths [21], when the structure of material is not significantly unchanged, can give the first sight into the fast motion of Li$^+$, the activation energy can be calculated by the empirical expression of Waugh and Fedin [22] or by fitting the formula introduced by Abragam [23] for motional narrowing of dipolar interaction.

2.2.3. Spin-lattice relaxation and spin-spin relaxation

Measurements on different relaxation rates, spin-lattice relaxation rates R_1 (in laboratory frame) and $R_{1\rho}$ (in rotating frame) and spin-spin relaxation rate R_2, provide Li-ion dynamics in different time scales (see Fig. 1). R_1 is sensitive to diffusive motion with jump rates for the range around Larmor frequency, which can be varied from 10 MHz to several hundred megahertz. $R_{1\rho}$ measurements with spin locking frequency and R_2 measurements can be used to detect slower motion in the kilohertz range [25]. Temperature dependent R_1 rates measurements are applied to calculate the activation energy (E_a). The two flanks of relaxation rates maximum are named as the low-T regime and the high-T regime respectively. Both of which fulfill the Arrhenius plots, then the two values of activation energy can be obtained by the adapting the following equation to the plots.

$$R_1 \propto \begin{cases} exp[E_{a\ high}/(k_B T)] & T > T_{max} \\ exp[-E_{a\ low}/(k_B T)] & T < T_{max} \end{cases}$$
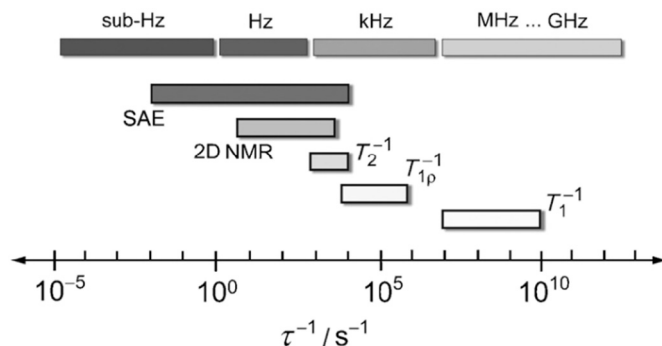

Fig. 1. Timescales of different microscopic NMR measurements. SAE denotes the spin alignment echo NMR. T_1^{-1} and $T_{1\rho}^{-1}$ denote the spin-lattice relaxation time in the laboratory and rotating frame respectively. T_2^{-1} is the spin-spin relaxation time. 2D NMR denotes the 2D EXSY NMR. The Figure is adapted from ref. [24].

$$E_{a\ low} = (\beta - 1)E_{a\ high}\ 1 < \beta \le 2$$

$E_{a\ low}$ is affected by correlation effects, thus, $E_{a\ high}$ is commonly used to represent the activation energy of ionic motion [21].

2.2.4. 2D exchange NMR and spin alignment echo NMR

But for ionic motions on the ultra-slow time scale, i.e., in the hertz and sub-hertz range, line shapes and relaxation rates are hardly accessible. But two-dimensional exchange (2D EXSY) NMR and spin alignment echo (SAE) NMR could make a difference for these slow motions in atomic scale. In 2D EXSY NMR spectra, the presence of cross peak indicates the two sites have a correlation, i.e. exchange of ions occurs between magnetically nonequivalent crystallographic sites and gives a direct evidence for Li$^+$ migration pathways. Furthermore, the jump rates could be acquired from ^{6}Li MAS 2D EXSY NMR spectra. But 2D EXSY NMR has to be performed with NMR peaks of different sites are well separated from each other. Spin Alignment Echo (SAE) NMR could work even when the different sites overlapped in the NMR spectra, and costs less time compared with 2D EXSY NMR [24].

3. Application of NMR in characterization of solid electrolytes

3.1. LISICON

Bruce et al. reported a novel lithium ion conductor—Li$_{14}$ZnGe$_4$O$_{16}$ [26], which has the same structure of γ-Li$_3$PO4, and named this material as LISICON (Lithium Super Ionic Conductor). The Li$_4$SiO$_4$-Li$_3$PO$_4$ solid solution is a typical LISICON-type ionic conductor. Different Si/P ratios samples were investigated by solid state NMR. ^{6}Li MAS NMR spectra revealed four environments of Li$^+$ (LiO$_n$ with n = 3, 4, 5, and 6). Dynamically, VT (varying temperatures) ^{7}Li relaxometry indicated that the minimum activation energy is achieved by the intermediate composition. That is in line with the best conductivity obtained from the composition of L$_{i3.5}$Si$_{0.5}$P$_{0.5}$O$_4$ by AC impedance [27]. However, its ionic conductivity is still far from the requirement of commercial LIBs.

LiBO$_2$ were added as an additive when synthesizing the 0.6Li$_4$SiO$_4$–0.4Li$_3$PO$_4$ samples, which resulted in the conductivity enhancement in this LISICON system [28]. Wang et al. [29] performed ^{11}B MAS NMR on probing the role of boron in the increase of the ionic conductivity. Obviously, two distinct positions of resonances at 20 ppm and 2 ppm were observed. The signal of 20 ppm exhibited a typical second-order quadrupolar characteristic, which indicated that the boron located in an asymmetrical environment at grain boundaries. The peak centered at 2 ppm without the second-order quadrupolar line shape was assigned to the tetrahedral site of boron, which inserted into the structure framework and replaced Si or P sites to form the structure like BO$_4$. According to the area of these two peaks, the authors concluded that most of boron located at grain boundaries and acted as a

sintering assistant for increasing the ionic conductivity. Moreover, when probing the amorphous phase like the glassy-type BO_3, which is invisible for XRD patterns, solid state NMR technique is regarded as a powerful technique that is not sensitive to the crystallinity of the materials.

3.2. Thio-LISICON

Based on LISICON materials, a series of novel lithium ion conductors 'Thio-LISICON' were synthesized by replacing O^{2-} with S^{2-}, which provided a much higher ionic conductivity due to a larger ionic radius and more polarizable character of S^{2-} [30]. This replacement weakens the bond strength between Li^+ and anions within the framework and improves the mobility of Li^+. In 2011, $Li_{10}GeP_2S_{12}$ (LGPS for short) with excellent conductivity was reported for the first time [31]. The conductivity of $1.2 \times 10^{-2}\,S\,cm^{-1}$ that is even better than some non-aqueous electrolytes [1].

Kuhn [7] carried out PFG-NMR and EIS techniques to probe the Li^+ dynamics in the electrolytes experimentally at the macroscopic time scale. The self-diffusion coefficients D based on different temperatures can be obtained. And then, the activation energy was calculated by the slope of the Arrhenius plot of temperature dependent self-diffusion coefficients. In this literature, only one activation energy of 0.23 eV was obtained, which was different from MD (molecular dynamics) simulation results [32,33] revealing that the migration pathway of Li^+ along an anisotropic 3D network consists of a one-dimensional path parallel to c-axis and an in-plane 2D pathways (ab plane) with the activation energy of 0.17 eV and 0.28 eV respectively. However electrochemical impedance spectroscopy showed the very close result with the activation energy of 0.22(1) eV, in line with PFG NMR results. Consequently, the authors claimed that no sign of anisotropy transport pathways was observed by PFG NMR and EIS.

Fig. 2a shows that a proposed Li-ion transport pathway of LGPS. Liang et al.[8]investigated the dynamics of LGPS with ^7Li spin-lock SLR and ^7Li SAE NMR. The correlation time (τ_{SAE}) was derived by fitting the SAE NMR curve with the following equation [34,35].

$$S_2(t_p = const., t_m) \propto exp\left[-\left(\frac{t_m}{t_{SAE}}\right)^\gamma\right]$$

t_m is the mixing time and γ is the exponential factor describing the SAE decay curve. As shown in Fig. 2b, there existed a no monotonous curve of logarithm of $1/\tau_{SAE}$ v.s. reciprocal of temperature. Thus, the activation energy of 0.16 eV and 0.26 eV could be deduced from the slopes of Arrhenius curve in different temperature regimes. In addition, ^7Li SLR NMR spectra in the rotating frame ($T_{1\rho}$) were performed to get more precise dynamic information. In the previous reports, the

relationship between SLR rates and spin-lock frequencies on the high-temperature side of SLR peak was used to investigate the dimensionality of ionic diffusion process [36–38]. Then, through the plot of ^7Li SLR rates v.s. reciprocal of temperature at different spin-lock frequencies, the authors observed the correlation of $R_{1\rho}$ and spin-lock frequency on the high-temperature flank of low-temperature peak, which indicated a 1D diffusion process of lithium ion in the low temperature. These results above agreed with the MD simulation results that proposed a 3D migration network of lithium ions, however, which did not coincide with the previous measurements for PFG-NMR and EIS. The cause of the difference is that PFG-NMR and EIS may bury some detailed information and obtain an average activation energy by considering these two measurements are only sensitive to long range diffusion. And it is worth noting that both of these two papers mentioned the existence of impurities from ^{31}P MAS NMR spectra. The investigation of Liang et al. [8] revealed that the impurity could decrease the conductivity of LGPS. But none of them put forward the specific composition of the impurities.

Based on different time and length scales, NMR techniques are able to obtain different results despite the same LGPS materials. PFG-NMR, in general, is performed to study the jump rates with time scales around $10^{-2} - 1$ s, corresponding to the long-range diffusion at the length scale of 10^{-6} m, including the 1D and 2D transport pathways in this case of LGPS. While SAE NMR and NMR relaxometry are microscopic NMR measurements with the length scale of 10^{-10} m, that is, atomic-scale. And the time scales could vary a large range from ultra-slow Li motion (sub-Hz) to fast Li motion (MHz). As a summary, Fig. 1 illustrates the common microscopic NMR techniques and their timescales.

3.3. NASICON-type material

NASICON-type materials are another kind of the most promising ionic conductors, which consist of corner-sharing PO_4 tetrahedra and MO_6 octahedra (e.g. Fig. 3a). When sodium ion is replaced by lithium ion in the classical NASICON structure, this kind of conductors will become lithium ion conductors [39]. As a typical NASICON material, $LiTi_2(PO_4)_3$(LTP) is limited by its low ionic conductivity. Much efforts toward tuning ionic conductivity have been carried out by the methods of aliovalent ions doping. For example, Aono et al. [40] reported that an enhancement of the ionic conductivity of LTP by substitution of M^{3+} for Ti^{4+} ($M^{3+} = Al^{3+}$, Sc^{3+}, Fe^{3+}, Y^{3+}). When M is Al or Sc, the maximum conductivity value of $7 \times 10^{-4}\,S\,cm^{-1}$can be realized at room temperature. The enhancement of conductivity was ascribed to the increasing density of the pellets. However, Wong et al. [41] identified that there existed the second phase of $AlPO_4$ which improved the sintering properties. Furthermore, Arbi et al. [42] found that the insulating phase like $AlPO_4$ could block the transport pathways of Li^+.

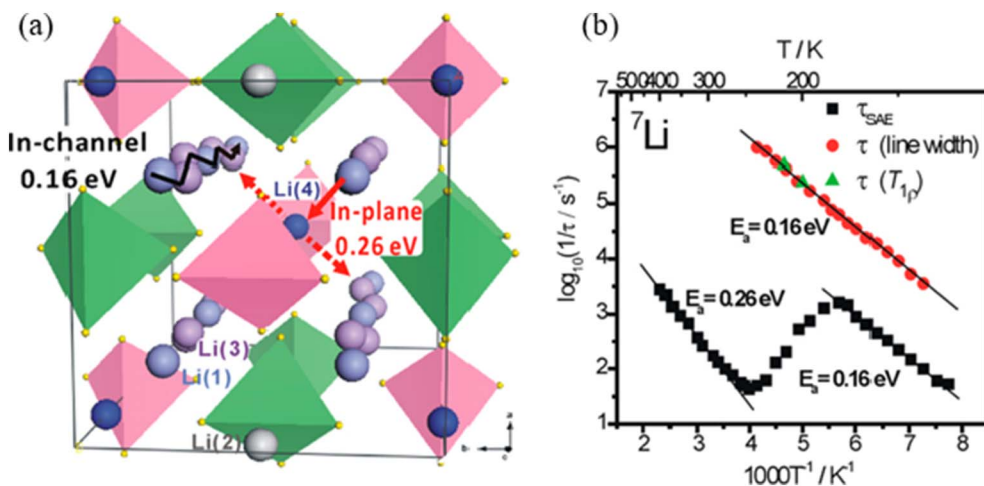**Fig. 2.** (a) 3D network of Li ion transport pathways. (b) ^7Li jump rates of LGPS extracted by $^6Li/^7Li$ SAE, ^7Li spin-lock SLR NMR, and line width. Figures are adapted from ref. [8].

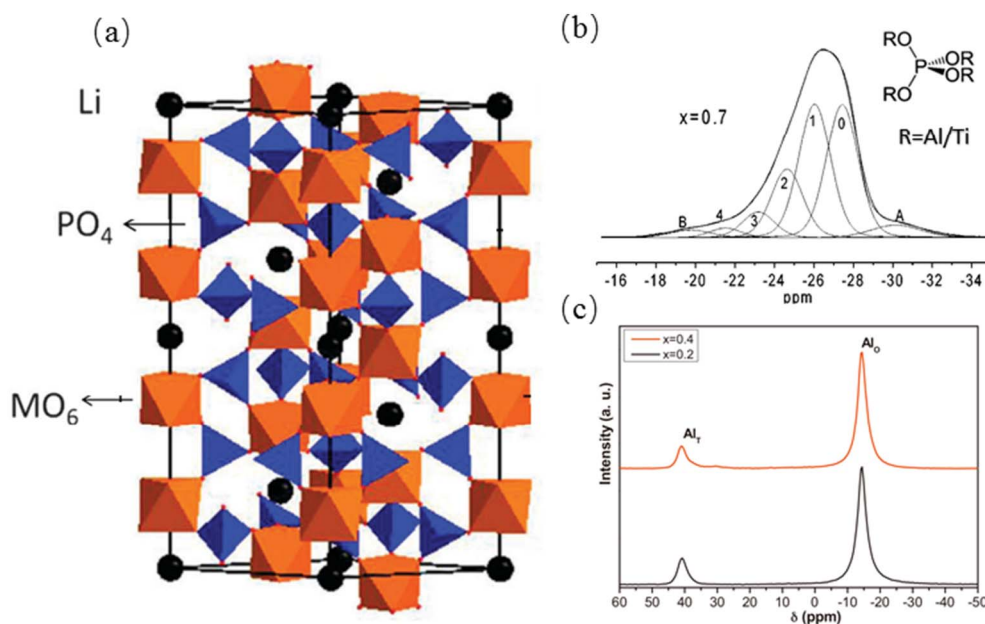Fig. 3. (a) crystal structure of NASICON-type lithium ion conductors [47]. (b) ^{31}P MAS NMR spectra with its deconvolution results for $Li_{1+x}Ti_{2-x}Al_x(PO_4)_3$ samples with x = 0.7. The label of 0, 1, 2, 3, 4 denote the environments of $P(OTi)_4$, $P(OTi)_3(OAl)_1$, $P(OTi)_2(OAl)_2$, $P(OTi)_1(OAl)_3$, and $P(OAl)_4$ respectively [42]. (c) ^{27}Al MAS NMR spectra of LATP [4].

Hence, in order to understand the role of aluminum in LATP, the structure should be discussed in details.

3.3.1. Structural investigation on LATP

In Al-substituted LTP material, two components were reported in ^{27}Al MAS NMR spectra in several works [4,42–44](Fig. 3c). The main signal centered at -15 ppm belongs to the Al/Ti substitution, which increases the Li^+ contents by charge compensation. The additional Li^+ occupies the Li3 sites due to the Li-Li repulsion and increase the vacancy of Li1 sites. Therefore, the conductivity of LATP is enhanced. Another peak centered at 40 ppm was assigned to either the formation of the second phase AlO_4 [45] or the Al/P substitution [46]. Though this assignment is still under discussion. As for ^{31}P MAS NMR, a single line of LTP centered at 27 ppm was observed. On substitution of Al, the single line becomes asymmetric broadening [43]. Arbi et al. [42] developed a model to explain the cause of broad signal. Structurally, PO_4 tetrahedron shares oxygen with four TiO_6 octahedra, which led to the formation of different environment for P labeled as $P(OTi)_4$, $P(OTi)_3(OAl)_1$, $P(OTi)_2(OAl)_2$, $P(OTi)_1(OAl)_3$, and $P(OAl)_4$ by Al/Ti substitution (see Fig. 3a).

Based on the model of ^{31}P environments developed by Arbi [42], quantitative analysis of LATP has been performed by ^{31}P MAS NMR. With different ^{31}P environments for 4Al, 3Al1Ti, 2Al2Ti, 1Al3Ti, 4Ti, the Al content was further deduced by the following equation, Where I_n (n = 0, 1, 2, 3, 4) represents the intensity of NMR signals associated with (4-n) Ti(n)Al environments.

$$\frac{Al^{3+}}{Ti^{4+}} = \frac{4I_4 + 3I_3 + 2I_2 + I_1}{I_3 + 2I_2 + 3I_1 + 4I_0} = \frac{x}{2-x}$$

Compared with nominal content deduced from chemical formula, the deviation was found when x > 0.2, indicating another second phase formed. Combined with XRD patterns, this deviation was ascribed to the formation of the second phase $AlPO_4$ and $Li_4P_2O_7$ which are located outside NASICON structure. At the same time, when x > 0.2, the impedance results indicated that the ionic conductivity decreased. Thus, the results concluded that the formation of the second phase may decrease the content of lithium ions in NASICON, and block the ionic transport channel.

In order to minimize the negative effect of the second phase, different synthetic methods were applied to suppress [48] or remove [45] the second phase $AlPO_4$ in LATP, which increase the grain boundary conductivity, leave the bulk conductivity unchanged. Thus, we can

infer that $AlPO_4$ phase exists in the grain boundary. Recently, Emery [49] et al. utilized a modified Pechini process to get $Li_{1.3}Al_{0.3}Ti_{1.7}(PO_4)_3$ powders without $AlPO_4$, which is validated by ^{27}Al MAS NMR spectra. Inspired by IR data [50,51]collected from LATP and combined with the large asymmetry parameter η_Q extracted from ^{27}Al NMR quadrupolar spectra, they concluded that Al doping could give rise to distortion in the P−O and Al−O bond [49]. In this case, the six components of ^{31}P MAS NMR were assigned to three pairs of lines for 0 Al, 1 Al, or 2Al in the neighborhood of P and the pairs of lines was ascribed to the long and short P−O bonds derived from the distortion of $M(PO_4)_3$ skeleton. And the authors proposed that the distortions might contribute to the enhancement of conductivity. Nevertheless, there is no other evidence to support this assumption yet as far as we know.

3.3.2. Ion dynamic process in LATP

Chandran et al. [44] systematically investigated Li^+ dynamic process in $Li_{1+x}Al_xTi_{2-x}(PO_4)_3$ (LATP, 0.0 < x < 1.0). When 0.35 < x < 0.5, fast migration of Li^+ was responsible for the overlap of ^{7}Li MAS NMR at room temperature. For the sample with x = 0.0, the line widths begin narrowing at around 220 K, while the sample with x = 0.35 reaches the extreme line widths limit. This phenomenon indicated a very fast motion of Li^+ within the latter material framework and Al doping did improve the conductivity.

NMR relaxometry is a useful method to determine diffusion parameters of lithium-ion conductors. Table 2 shows the $E_{a\ low}$, $E_{a\ high}$ and T_{max} for $Li_{1+x}Al_xTi_{2-x}(PO_4)_3$. The minimum of $E_{a\ high}$ and T_{max} is observed when 0.35 < x < 0.5. This agrees with the reported value of x for the best conductivity in LATP [53,54]. The difference between $E_{a\ high}$ and $E_{a\ low}$ is ascribed to the correlation effects that decrease the $E_{a\ low}$. For x = 0.1, two SLR rate peaks were observed, and for x = 0.2, the low temperature regime becomes broader (see black line in Fig. 4a). On the basis of analysis of Fig. 4a, the authors draw a conclusion that there

Table 2
Activation energy calculated from the two flanks of diffusion induced by ^{7}Li SLR rate maximum and the T_{max} at which the maximum relaxation rate was reached [44].

x	0.00	0.10	0.20	0.35	0.50	0.70	1.00
$E_{a\ high}$/eV	0.41	0.37	0.30	0.29	0.29		
$E_{a\ low}$/eV	0.41	0.29				0.40	0.33
T_{max}/K	380	280, 245	245	213	213	423	413

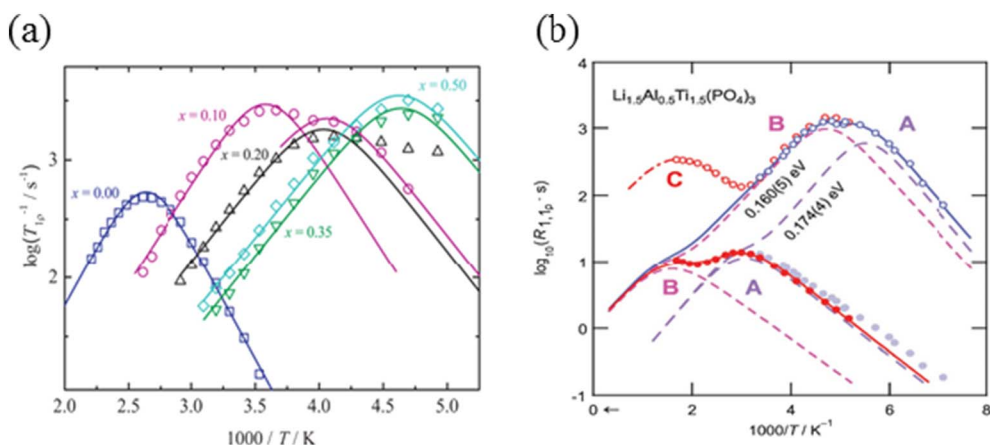**Fig. 4.** ^{7}Li spin-lattice relaxation rates in rotating frame for LATP samples with (a) x = 0.0, 0.10, 0.20, 0.35, and 0.5 in ref. [44]; (b) R_1 and $R_{1\rho}$ rates v.s. inverse temperature of $Li_{1.5}Al_{0.5}Ti_{1.5}(PO_4)_3$ in ref. [55].

may exist two diffusion processes, which was similar to that reported by Wilkening [55]. They found that there were two distinct peaks rendered by two dashed lines shown in Fig. 4b, representing two diffusion processes marked as A and B. The activation energy derived from high-temperature flank of peak A was fitted as 0.17 eV, and peak B was 0.16 eV. The difference of the activation energy coming from the two works might be ascribed to the structural differences in LATP prepared, which would result in different migration model, the vacancy migration model and the interstitial migration model respectively [56].

^{6}Li 2D EXSY NMR spectra were also performed on the LATP with x = 0.7 [44]. Two broad signals around 0 ppm which were assigned to the second phase showed a cross peak, and the exchange rate is 4 s^{-1}, which represented an ultraslow exchange between these two Li$^+$ sites. Thus, the authors concluded that the formation of the second phase at the expense of LATP phase might restrain the transport of ions and influence ionic conductivity. This result is in line with the Arbi's results [40]. Besides, Emery et al. [49] measured NMR relaxation times—T_1 (^{6}Li), T_1 (^{7}Li), T_{1Q} (^{7}Li), T_2 (^{7}Li) and $T_{1\rho}$ (^{7}Li) in LATP, which indicated an anisotropy migration pathway of Li$^+$ within LATP framework. The T_1 and T_2 relaxation of ^{31}P and ^{27}Al revealed no movement of these two nuclei [52].

In a short summary, NMR methods provide a solid evidence of the formation of the second phase and different Al coordination environment [57]. The information extracted from NMR measurements, as a complementary with EIS, can quantitatively analyze the microscopic behavior of Li ions such as the jump rates.

3.4. Garnet-type materials

Since its discovery, garnet-type materials exhibit promising electrochemical properties, especially relatively high ionic conductivity. The chemical formula of the traditional garnet-type ionic conductors is $X_nA_3B_2O_{12}$, where X denotes Li$^+$. By aliovalent ions doping, the content of n could vary from 3 to 7. According to the lithium contents, garnet type materials could be sorted into three groups, including $Li_3Ln_3Te_2O_{12}$(Ln = Y, Pr, Nd) (Li3 group), $Li_5La_3M_2O_{12}$(M = Nb, Ta, Sb, Bi) (Li5 group) and $Li_7La_3C_2O_{12}$(C = Zr, Sn, Hf) (Li7 group). Kuhn et al. summarized several dynamic behaviors of Li ions several years ago [21]. In the following section, we give a short overview of the newest investigation on the transport properties of lithium ions in garnet-type ionic conductors.

3.4.1. Li3 group

$Li_3Ln_3Te_2O_{12}$, due to its low lithium ion content, possesses poor conductivity. In the aspect of structure, all the Li$^+$ occupy tetrahedron sites, in which the mobility is limited by the high activation energy. Only a single resonance around 10 ppm was observed in ^{6}Li MAS NMR, which belonged to the ordered arrangement of tetrahedron sites [57].

Another resonance which is assigned to distorted octahedra site appears in 25 ppm with Te and Sb doping, accompanied by conductivity enhancement. The similar new resonance peak was observed by Cussen [58]. The validation of the distorted octahedral Li$^+$ site had a positive impact on conductivity were also supported by neutron diffraction(ND) [59] and density function simulation results [60].

3.4.2. Li5 group

$Li_5La_3Nb_2O_{12}$, as the first reported garnet-type ionic conductor [61], was investigated by ^{6}Li NMR in details [62]. From ^{6}Li MAS NMR spectra, the intensity of signal centered at 0.7 ppm (representing Li in octahedral sites) was so strong that another signal centered at −0.2 ppm (representing Li in tetrahedral sites) was partly buried. For a better understanding the dynamics of tetrahedral sites, considering the ^{6}Li MAS NMR spectra have a better resolution, but lower sensitivity than that of ^{7}Li spectra, temperature dependent ^{7}Li-^{6}Li CPMAS NMR was performed to enhance the sensitivity of ^{6}Li. With CPMAS, magnetization can be transferred from the more abundant ^{7}Li to the less abundant ^{6}Li. So, the ^{6}Li MAS NMR spectra can be collected at a higher magnetization level. The efficiency of cross polarization decreases with lithium ions movement, which results in the heteronuclear dipolar averaged. Therefore, the signal of octahedral sites with high mobility was suppressed. As shown in Fig. 5, the upfield signal of tetrahedron sites become more distinctive with CPMAS techniques. When varying temperature, Fig. 5b showed an almost unchanged line width of the upfield signal, suggesting that the low mobility of these sites. Furthermore, in ^{7}Li-^{6}Li CPMAS 2D EXSY NMR spectra, there only existed diagonal peaks of LiO$_6$ and LiO$_4$ with mixing time of 1 s. The absence of cross peaks indicated that there was no jump between the two lithium sites within one second.

3.4.3. Li7 group

$Li_7La_3Zr_2O_{12}$ (LLZO) with cubic symmetry was firstly reported by Murugan [63] in 2007, which has the highest ionic conductivity conductor in garnet series. Fig. 6 illustrates the transport path of Li$^+$ and the structure of the LLZO. However, as different from that the tetrahedral sites (24d) are not involved in the lithium ion transport pathway in Li3 and Li5 group materials. Neutron Powder Diffraction (NPD) [64] and first-principle calculations [60] indicated that lithium ions can jump from one tetrahedral site to the neighboring octahedral site in Li7 group materials. In order to confirm such a lithium ion transport pathway, 2D EXSY NMR [5] and SAE NMR [65] were performed.

As shown in Fig. 7a, Wang et al. [5] performed ^{6}Li MAS NMR (top curve) on $Li_{7-2x-3y}Al_yLa_3Zr_{2-x}W_xO$ (x = 0.5), where only two resonances (1.9 ppm and 0.8 ppm) was observed for identifying three crystallographic Li sites (24d, 48 g, and 96 h). The authors utilized a new pulse sequence by differentiating T_1 to suppress the strong signal centered at 1.9 ppm. After this processing, there appears a new signal
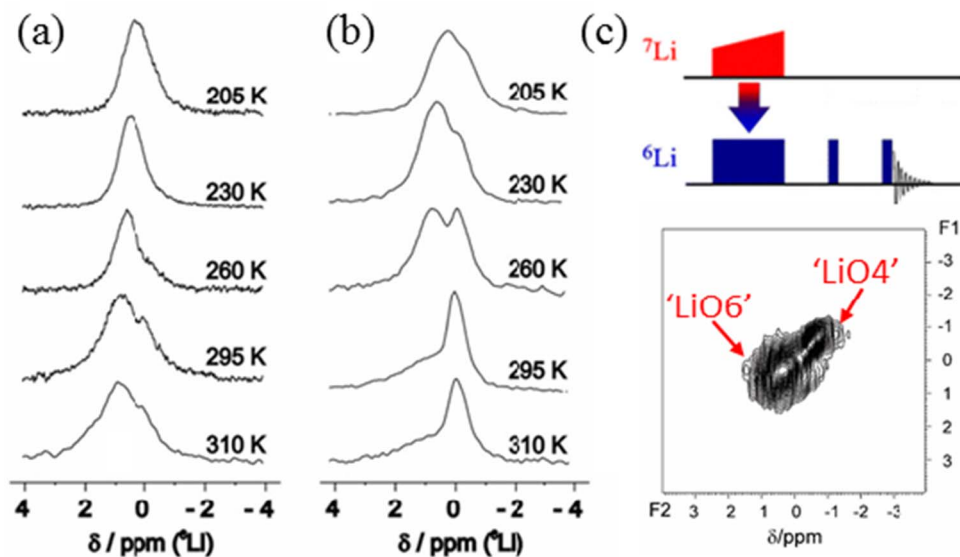
Fig. 5. (a) ^{6}Li MAS NMR spectra, (b) ^{7}Li-^{6}Li CPMAS NMR spectra with the signal of octahedral sites suppressed, and (c) ^{7}Li-^{6}Li CPMAS 2D EXSY spectra with mixing time of 1 s acquired from the sample of Li$_5$La$_3$Nb$_2$O$_{12}$. Figures are adapted from ref. [62].

around 1.5 ppm (see bottom curve of Fig. 7a), that may be covered by the strong signal at 1.9 ppm with the measurement of the single pulse. Therefore, three NMR signals can be distinguished. And thereafter, ^{6}Li-^{6}Li EXSY NMR was performed after suppressing the signal of octahedral to confirm the assignment of Li sites where the presence of cross peak demonstrates that there existed a correlation between the peaks of 1.5 ppm and 0.8 ppm. Considering the transportation of Li$^+$ was along the 24d-96 h-48 g-96 h-24d pathway and 24d sites were responsible for 0.8 ppm, the peak of 1.5 ppm was ascribed to 96 h sites, and the 1.9 ppm to 48 g sites. It provides a direct evidence that supports 24d sites were involved in lithium ions migration and reasonably connect NMR peaks with crystallographic sites. Such idea of differentiating weak peak in an overlapping peak by suppressing strong signals was also reported by Wullen [62]. In short, both of these two works utilize the difference of dynamical characteristic to differentiate different Li + sites from NMR spectra. Similarly, SAE NMR can also be used to investigate the jump path between different electrically inequivalent sites. e.g. Wilkening et al. [65] performed multiple NMR measurements to study Li ions dynamics in Li$_{6.5}$La$_3$Zr$_{1.75}$Mo$_{0.25}$O$_{12}$. Among them, the SAE NMR curve showed two-steps damping behavior, indicated that both of 96 h and 24d sites were involved in lithium ion transport path.

In fact, the cubic phase LLZO is not so stable as tetragonal phase whose conductivity is lower about 2 orders magnitudes. There are some

works reported that Al and Ga can stabilize the cubic phase of LLZO [66,67]. However, the mechanisms of stable the cubic phase and the effect of doping element on ionic conductivity need more detailed study. The AC impedance showed that the ionic conductivity of Li$_{6.75}$La$_3$Zr$_{1.75}$Ta$_{0.25}$O$_{12}$ is higher than Ga- and Al-doped LLZTO [68]. Besides, the results [69] from measurements of ^{7}Li NMR relaxometry, line shape and impedance spectroscopy showed improved conductivity in Ga-doped LLZO compared to Al-doped one. In general, the introduction of Ga and Al may have a negative effect on the transport of lithium ions from a structural perspective at different degrees, respectively.

Multinuclear MAS NMR experiments were performed in order to give a reasonable explanation to the changes of ionic conductivity with Ga, Al doping. ^{27}Al MAS NMR [70,71] and ^{71}Ga MAS NMR showed that Li sites occupied by Ga and Al, which may act as a blocking barrier in the transport path of lithium ions. As for Ga-doped and Al-doped LLZO, Allen's results [68] indicated that there may be a different site preference of Ga and Al. ^{71}Ga MAS NMR spectrum showed a single line [72] while ^{27}Al MAS NMR with two or three lines [70,71]. Rettenwander [73] ascribed these two lines to the 24d and 96 h sites which occupied by Al^{3+}. The occupancy of 24d sites by Al^{3+} is also confirmed by Xu [71] and Charles [70], using ^{27}Al MAS NMR and MQMAS NMR respectively. Considering the Li$^+$ transport pathway
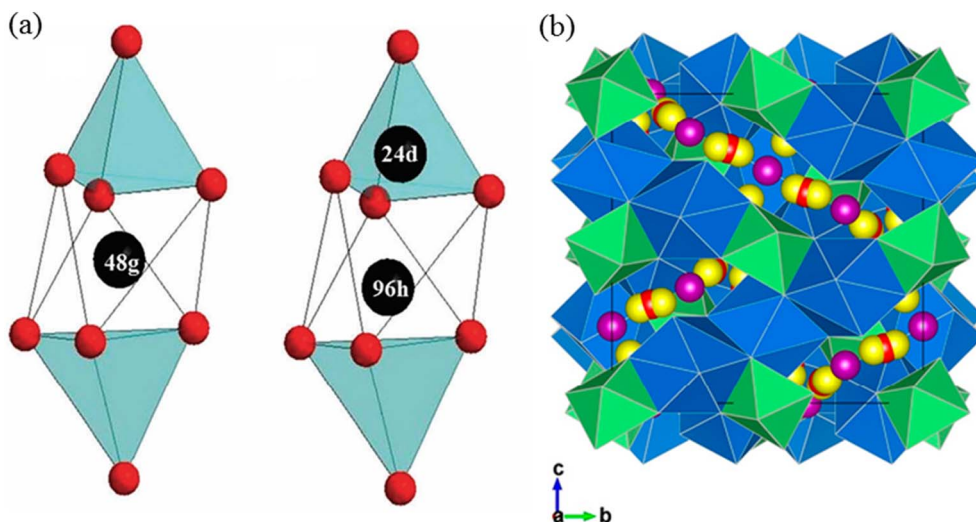

Fig. 6. (a) Li sites in the garnet-type structure. (b) transport path of Li$^+$ and crystal structure of cubic LLZO. Blue dodecahedra denote the LaO$_8$, and green octahedron denotes the ZrO$_6$. Purple, red, and yellow spheres correspond to lithium ions located at 24d, 48 g, 96 h sites respectively. Figures are adapted from ref. [47,66]. (For interpretation of the references to colour in this figure legend, the reader is referred to the web version of this article.)
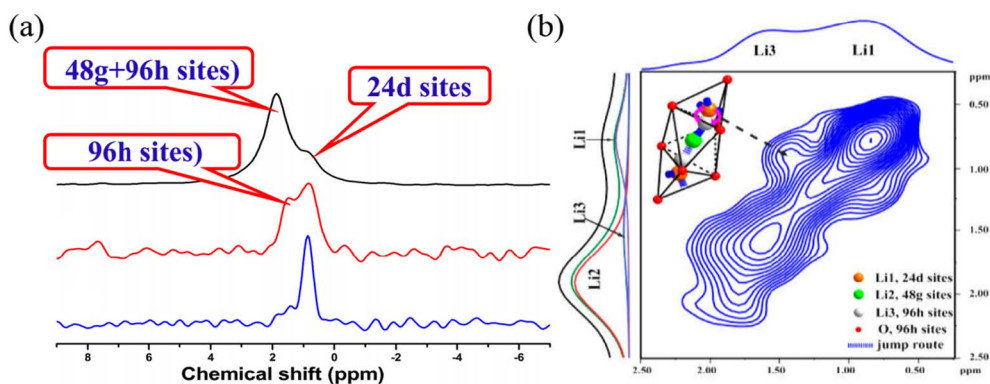
4. Summary and outlook

The development of safer solid-state lithium batteries requires a deep understanding of the structure of the materials and the dynamic transport processes of lithium ion, which plays a guiding role in the design and fabrication of an ideal lithium ion conductor. Solid state nuclear magnetic resonance spectroscopy can not only detect the local structure efficiently, but also directly study the ion dynamics from the microscopic (or atomic) perspective.

LGPS is a typical LISICON-type material which possesses the highest ionic conductivity over all the lithium ion conductors at present. The theoretical calculation revealed the presence of two different migration pathways of lithium ions. However, the commonly used electrochemical characterization methods such as EIS can only measure apparent ionic conductivity and electrochemical diffusion coefficients of Li ions. Herein, the NMR results not only confirm there exists two migration pathways experimentally, as well as the dynamic information at localized Li sites.

LATP is the material with the highest lithium ion conductivity in NASICON-type lithium ion conductors. The formation of the second phase (either amorphous or crystalline phase) was analyzed by the combination of NMR and XRD patterns. The evolution of ion jump rates was revealed by SLR NMR, from which the two migration pathways were observed.

In garnet-type lithium ion conductors, three crystallographic sites for lithium ions were found in LLZO, i.e. 24d, 48 g and 96 h. The number of lithium ions occupying at 96 h/48 g sites played a key role in improving the ionic conductivity. SAE NMR and 2D EXSY NMR results revealed that the 24d sites are involved in the transport of lithium ions, as a junction site. Besides, in Al- and Ga-doped LLZO, MAS NMR results indicated that the lithium sites can be occupied by doping elements, which explained why the ionic conductivity of doped LLZTO was lower than pure LLZTO [68].

As mentioned above, for all solid-state lithium ion batteries, the ionic conductivity is not the only limiting factor. The interface between solid state electrolytes and electrodes must be considered due to high resistances and impressible properties at this solid/solid interface. In this regard, NMR techniques have been starting introduced in this important topic. E.g. Yu et al. [78] took advantage of different chemical shifts of lithium ions between Li_6PS_5Cl and Li_2S, to quantified the Li ion transport over the Li_6PS_5Cl-Li_2S interface through performing exchange NMR methods. However, it is noteworthy that current applications of NMR techniques in solid electrolytes are carried out mostly on the basis of ex-situ measurements without the presence of external electric field and the species concentration difference. In the practical system of all solid-state batteries, the real diffusion patterns of lithium ions need to be characterized and understood by in situ NMR methods. Therefore, how to develop an efficient model to simulate the transport of lithium ions in the practical system, and certainly to develop real-time or operando-NMR experimental set-up for working solid-state batteries is the

Fig. 8. ^{71}Ga MAS NMR spectra in $Li_{5.8}Ga_{0.40}Al_{0.00}La_3Zr_2O_{12}$ measured at 9.4 T (left) and 21.1 T (right). The figure is adapted from ref. [76]

within LLZO framework, 24d was thought to be a junction site (see Fig. 6b). Thus, the presence of Al^{3+} at 24d sites might block the transport pathway of Li^+ and decrease the conductivity. As for the single line in ^{71}Ga MAS NMR spectrum, Howard [72] assigned the signal around 221 ppm to the 24d site. However, Rettenwander et al. [74] simulated ^{71}Ga MAS NMR and gained an asymmetry parameter η_Q of 0.46. In view of the low symmetry of 96 h site in LLZO, the authors proposed that Ga only occupied the 96 h site. Consider the Al-doped LLZO with Al^{3+} may occupy the junction site (24d) as a blockade of lithium ion transport-path, Rettenwander [73] thought it may responsible for the lower ionic conductivity of Al-LLZO. However, recently, high resolution ^{71}Ga MAS NMR spectra were performed by ultrahigh magnetic fields (21.1 T) [75]. Because the second order quadrupole interaction decreased when meeting high magnetic fields, it could get a better resolved spectrum, so that two components could be identified separately of 243 ppm assigned to 96 h and 193 ppm assigned to 24d (see Fig. 8). It should be pointed out that the high magnetic fields could make an advantage on increasing the resolution when studying these quadrupole nuclei with strong second-order quadrupole interaction. However, the achievement is at the expense of losing the information from quadrupole shape [76].

As for site preferences, Al and Ga behave as the same tendency seen from NMR spectra [75]. Moreover, authors tend to connect the conductivity enhancement with the increase of lattice size, because Ga^{3+} has a larger ionic radius than Al^{3+}. However, to the best of our knowledge, the introduction of Ga could decrease the interfacial resistance [77], which may be part of the reasons for the enhancement of total conductivity.

premise on the way to understand the phenomena in "closed" battery system. In addition, new NMR techniques such as NMR imaging techniques with good resolution could provide more useful information for the analysis of decay of the solid electrolytes or even breakdown of the batteries.

Acknowledgment

References

[1] J.C. Bachman, S. Muy, A. Grimaud, H.H. Chang, N. Pour, S.F. Lux, O. Paschos, F. Maglia, S. Lupart, P. Lamp, L. Giordano, Y. Shao-Horn, Chem. Rev. 116 (1) (2016) 140–162.
[2] A. Kuhn, J. Kohler, B.V. Lotsch, Phys. Chem. Chem. Phys. 15 (28) (2013) 11620–11622.
[3] K. Arbi, M. Hoelzel, A. Kuhn, F. Garcia-Alvarado, J. Sanz, Phys. Chem. Chem. Phys. 16 (34) (2014) 18397–18405.
[4] K. Arbi, W. Bucheli, R. Jiménez, J. Sanz, J. Eur. Ceram. Soc. 35 (5) (2015) 1477–1484.
[5] D. Wang, G. Zhong, W.K. Pang, Z. Guo, Y. Li, M.J. McDonald, R. Fu, J.-X. Mi, Y. Yang, Chem. Mater. 27 (19) (2015) 6650–6659.
[6] D. Wang, G. Zhong, O. Dolotko, Y. Li, M.J. McDonald, J. Mi, R. Fu, Y. Yang, J. Mater. Chem. A 2 (47) (2014) 20271–20279.
[7] A. Kuhn, V. Duppel, B.V. Lotsch, Energy Environ. Sci. 6 (12) (2013) 35–48.
[8] X. Liang, L. Wang, Y. Jiang, J. Wang, H. Luo, C. Liu, J. Feng, Chem. Mater. 27 (16) (2015) 5503–5510.
[9] L.S. Cahill, R.P. Chapman, J.F. Britten, G.R. Goward, J. Phys. Chem. B 110 (2006) 7171–7177.
[10] J. Cabana, N. Dupre, G. Rousse, C. Grey, M. Palacin, Solid State Ionics 176 (29–30) (2005) 2205–2218.
[11] L.J.M. Davis, I. Heinmaa, G.R. Goward, Chem. Mater. 22 (3) (2010) 769–775.
[12] V.W. Verhoeven, I.M. de Schepper, G. Nachtegaal, A.P. Kentgens, E.M. Kelder, J. Schoonman, F.M. Mulder, Phys. Rev. Lett. 86 (19) (2001) 4314–4317.
[13] M. Wilkening, P. Heitjans, J. Phys. Condens. Matter 18 (43) (2006) 9849–9862.
[14] O. Pecher, J. Carretero-González, K.J. Griffith, C.P. Grey, Chem. Mater. 29 (1) (2017) 213–242.
[15] M. Wilkening, A. Kuhn, P. Heitjans, Phys. Rev. B 78 (5) (2008) 054303.
[16] M. Wilkening, W. Kuchler, P. Heitjans, Phys. Rev. Lett. 97 (6) (2006) 065901.
[17] M. Wilkening, P. Heitjans, Phys. Rev. B 77 (2) (2008) 024311.
[18] M. Wilkening, D. Gebauer, P. Heitjans, J. Phys. Condens. Matter 20 (2) (2008) 022201.
[19] E.O. Stejskal, J.E. Tanner, J. Chem. Phys. 42 (1) (1965) 288–292.
[20] J.E. Tanner, J. Chem. Phys. 52 (5) (1970) 2523–2526.
[21] A. Kuhn, S. Narayanan, L. Spencer, G. Goward, V. Thangadurai, M. Wilkening, Phys. Rev. B 83 (9) (2011) 094302.
[22] J. Waugh, E. Fedin, Sov. Phys. Solid State 4 (8) (1963) 1633–1636.
[23] A. Abragam, The Principles of Nuclear Magnetism, Oxford University Press, 1961.
[24] M. Wilkening, P. Heitjans, ChemPhysChem 13 (1) (2012) 53–65.
[25] S.M. E, M.K.J. D, Pergamon Materials Series, (2002).
[26] H.-P. Hong, Mater. Res. Bull. 13 (2) (1978) 117–124.
[27] Y.W. Hu, I. Raistrick, R.A. Huggins, J. Electrochem. Soc. 124 (8) (1977) 1240–1242.
[28] L. Zhang, L. Cheng, J. Cabana, G. Chen, M.M. Doeff, T.J. Richardson, Solid State Ionics 231 (2013) 109–115.
[29] D. Wang, G. Zhong, Y. Li, Z. Gong, M.J. McDonald, J.-X. Mi, R. Fu, Z. Shi, Y. Yang, Solid State Ionics 283 (2015) 109–114.
[30] R. Chen, W. Qu, X. Guo, L. Li, F. Wu, Mater. Horiz. 3 (6) (2016) 487–516.
[31] N. Kamaya, K. Homma, Y. Yamakawa, M. Hirayama, R. Kanno, M. Yonemura, T. Kamiyama, Y. Kato, S. Hama, K. Kawamoto, A. Mitsui, Nat. Mater. 10 (9) (2011) 682–686.
[32] Y. Mo, S.P. Ong, G. Ceder, Chem. Mater. 24 (1) (2012) 15–17.
[33] S. Adams, R. Prasada Rao, J. Mater. Chem. 22 (16) (2012) 76–87.
[34] R. Bohmer, J. Magn. Reson. 147 (1) (2000) 78–88.
[35] J. Jeener, P. Broekaert, Phys. Rev. 157 (2) (1967) 232–240.
[36] A. Kuhn, P. Sreeraj, R. Pöttgen, H.-D. Wiemhöfer, M. Wilkening, P. Heitjans, J. Am. Chem. Soc. 133 (29) (2011) 11018–11021.
[37] B. Yager, J. Nyéki, A. Casey, B. Cowan, C. Lusher, J. Saunders, Phys. Rev. Lett. 111 (21) (2013) 215303.
[38] C. Sholl, J. Phys. C Solid State Phys. 14 (4) (1981) 447–464.
[39] C.R. Mariappan, C. Yada, F. Rosciano, B. Roling, J. Power Sources 196 (15) (2011) 6456–6464.
[40] H. Aono, E. Sugimoto, Y. Sadaoka, N. Imanaka, G. Adachi, J. Electrochem. Soc. 137 (4) (1990) 1023–1027.
[41] P.J.N. Shan Wong, bA.S. Best, bK.M. Nairn, aD.R. MacFarlaneb, Maria Forsyth, J. Mater. Chem. 8 (10) (1998) 2199–2203.
[42] K. Arbi, S. Mandal, J.M. Rojo, J. Sanz, Chem. Inform. 33 (24) (2010).
[43] M.F.K.M. Nairn, M. Greville, D.R. MacFarlaneb, M.E. Smithc, Solid State Ionics 86–88 (1996) 1397–1402.
[44] C. Vinod Chandran, S. Pristat, E. Witt, F. Tietz, P. Heitjans, J. Phys. Chem. C 120 (16) (2016) 8436–8442.
[45] A. Best, M. Forsyth, D. MacFarlane, Solid State Ionics 136 (2000) 339–344.
[46] K. Arbi, M. Lazarraga, D. Ben Hassen Chehimi, M. Ayadi-Trabelsi, J. Rojo, J. Sanz, Chem. Mater. 16 (2) (2004) 255–262.
[47] V. Thangadurai, S. Narayanan, D. Pinzaru, Chem. Soc. Rev. 43 (13) (2014) 4714–4727.
[48] K. Arbi, R. Jimenez, T. Šalkus, A.F. Orliukas, J. Sanz, Solid State Ionics 271 (2015) 28–33.
[49] J. Emery, T. Šalkus, M. Barré, J. Phys. Chem. C 120 (46) (2016) 26235–26243.
[50] N. Kosova, E. Devyatkina, A. Stepanov, A. Buzlukov, Ionics 14 (4) (2008) 303–311.
[51] N. Kosova, D.I. Osintev, N.F. Uvarov, E.T. Devyakkina, Chem. Sustain. Dev. 13 (2005) 253–260.
[52] J. Emery, T. Šalkus, M. Barré, J. Phys. Chem. C 121 (1) (2017) 246–254.
[53] D. Rettenwander, A. Welzl, S. Pristat, F. Tietz, S. Taibl, G. Redhammer, J. Fleig, J. Mater. Chem. A 4 (4) (2016) 1506–1513.
[54] H. Morimoto, M. Hirukawa, A. Matsumoto, T. Kurahayashi, N. Ito, S.-i. Tobishima, Electrochemistry 82 (10) (2014) 870–874.
[55] V. Epp, Q. Ma, E.M. Hammer, F. Tietz, M. Wilkening, Phys. Chem. Chem. Phys. 17 (48) (2015) 32115–32121.
[56] B. Lang, B. Ziebarth, C. Elsässer, Chem. Mater. 27 (14) (2015) 5040–5048.
[57] O.C. Michael, P. Andrew, S. Powell, Jeremy J. Titman, George Z. Chen, E.J. Cussen, Chem. Mater. 20 (6) (2008) 2360–2369.
[58] E.J. Cussen, J. Mater. Chem. 20 (25) (2010) 5167–5173.
[59] Y. Li, J.-T. Han, C.-A. Wang, H. Xie, J.B. Goodenough, J. Mater. Chem. 22 (30) (2012) 15357–15361.
[60] M. Xu, M.S. Park, J.M. Lee, T.Y. Kim, Y.S. Park, E. Ma, Phys. Rev. B 85 (5) (2012).
[61] V. Thangadurai, H. Kaack, W.J. Weppner, J. Am. Ceram. Soc. 86 (3) (2003) 437–440.
[62] L. van Wullen, T. Echelmeyer, H.W. Meyer, D. Wilmer, Phys. Chem. Chem. Phys. 9 (25) (2007) 3298–3303.
[63] R. Murugan, V. Thangadurai, W. Weppner, Angew. Chem. 46 (41) (2007) 7778–7781.
[64] J. Han, J. Zhu, Y. Li, X. Yu, S. Wang, G. Wu, H. Xie, S.C. Vogel, F. Izumi, K. Momma, Y. Kawamura, Y. Huang, J.B. Goodenough, Y. Zhao, Chem. Commun. 48 (79) (2012) 9840–9842.
[65] P. Bottke, D. Rettenwander, W. Schmidt, G. Amthauer, M. Wilkening, Chem. Mater. 27 (19) (2015) 6571–6582.
[66] H. Buschmann, J. Dolle, S. Berendts, A. Kuhn, P. Bottke, M. Wilkening, P. Heitjans, A. Senyshyn, H. Ehrenberg, A. Lotnyk, V. Duppel, L. Kienle, J. Janek, Phys. Chem. Chem. Phys. 13 (43) (2011) 19378–19392.
[67] E. Rangasamy, J. Wolfenstine, J. Sakamoto, Solid State Ionics 206 (2012) 28–32.
[68] J.L. Allen, J. Wolfenstine, E. Rangasamy, J. Sakamoto, J. Power Sources 206 (2012) 315–319.
[69] R. Wagner, G.J. Redhammer, D. Rettenwander, A. Senyshyn, W. Schmidt, M. Wilkening, G. Amthauer, Chem. Mater. 28 (6) (2016) 1861–1871.
[70] C.A. Geiger, E. Alekseev, B. Lazic, M. Fisch, T. Armbruster, R. Langner, M. Fechtelkord, N. Kim, T. Pettke, W. Weppner, Inorg. Chem. 50 (3) (2011) 1089–1097.
[71] B. Xu, H. Duan, W. Xia, Y. Guo, H. Kang, H. Li, H. Liu, J. Power Sources 302 (2016) 291–297.
[72] M.A. Howard, O. Clemens, E. Kendrick, K.S. Knight, D.C. Apperley, P.A. Anderson, P.R. Slater, Dalton Trans. 41 (39) (2012) 12048–12053.
[73] D. Rettenwander, P. Blaha, R. Laskowski, K. Schwarz, P. Bottke, M. Wilkening, C.A. Geiger, G. Amthauer, Chem. Mater. 26 (8) (2014) 2617–2623.
[74] D. Rettenwander, C.A. Geiger, M. Tribus, P. Tropper, G. Amthauer, Inorg. Chem. 53 (12) (2014) 6264–6269.
[75] D. Rettenwander, J. Langer, W. Schmidt, C. Arrer, K.J. Harris, V. Terskikh, G.R. Goward, M. Wilkening, G. Amthauer, Chem. Mater. 27 (8) (2015) 3135–3142.
[76] D. Rettenwander, R. Wagner, J. Langer, M.E. Maier, M. Wilkening, G. Amthauer, Eur. J. Mineral. 28 (3) (2016) 619–629.
[77] D. Rettenwander, G. Redhammer, F. Preishuber-Pflugl, L. Cheng, L. Miara, R. Wagner, A. Welzl, E. Suard, M.M. Doeff, M. Wilkening, J. Fleig, G. Amthauer, Chem. Mater. 28 (7) (2016) 2384–2392.
[78] C. Yu, S. Ganapathy, N.J.J. de Klerk, I. Roslon, E.R.H. van Eck, A.P.M. Kentgens, M. Wagemaker, J. Am. Chem. Soc. 138 (35) (2016) 11192–11201.